Mon. Not. R. Astron. Soc. **000**, 1–?? (XXXX) Printed 12 January 2015 (MN LATEX style file v2.2)

Clues on void evolution III: Structure and dynamics in void shells

Andrés N. Ruiz[1,2⋆], Dante J. Paz[1,2], Marcelo Lares[1,2], Heliana E. Luparello[1], Laura Ceccarelli[1,2], Diego García Lambas[1,2]

[1] *Instituto de Astronomía Teórica y Experimental, CONICET–UNC, Laprida 854, X5000BGR, Córdoba, Argentina.*
[2] *Observatorio Astronómico de Córdoba, Universidad Nacional de Córdoba, Laprida 854, X5000BGR, Córdoba, Argentina.*

Accepted XXX. Received XXX; in original form XXX

ABSTRACT

Inspired on the well known dynamical dichotomy predicted in voids, where some underdense regions expand whereas others collapse due to overdense surrounding regions, we explored the interplay between the void inner dynamics and its large scale environment. The environment is classified depending on its density as in previous works. We analyse the dynamical properties of void-centered spherical shells at different void-centric distances depending on this classification. The above dynamical properties are given by the angular distribution of the radial velocity field, its smoothness, the field dependence on the tracer density and shape, and the field departures from linear theory. We found that the velocity field in expanding voids follows more closely the linear prediction, with a more smooth velocity field. However when using velocity tracers with large densities such deviations increase. Voids with sizes around $18h^{-1}$Mpc are in a transition regime between regions with expansion overpredicted and underpredicted from linear theory. We also found that velocity smoothness increases as the void radius, indicating the laminar flow dominates the expansion of larger voids (more than $18h^{-1}$Mpc). The correlations observed suggest that nonlinear dynamics of the inner regions of voids could be dependent on the evolution of the surrounding structures. These also indicate possible scale couplings between the void inner expansion and the large scale regions where voids are embedded. These results shed some light to the origin of nonlinearities in voids, going beyond the fact that voids just quickly becomes nonlinear as they become emptier.

Key words: large–scale structure of the universe - methods: numerical - methods: statistical

1 INTRODUCTION

Voids are prominent features of the large-scale structure of the Universe since they are surrounded by elongated filaments, sheetlike walls and dense compact clusters, setting the pattern of the cosmic web (Colless et al. 2001; Colless et al. 2003; Tegmark et al. 2004; Huchra et al. 2005). Also, voids are likely to determine large-scale velocity fields by their radial flows of mass and galaxies induced by the local mass underdensity (Bertschinger 1985; Melott & Shandarin 1990; Mathis & White 2002; Colberg et al. 2005a; Shandarin et al. 2006; Platen et al. 2008; Aragon-Calvo & Szalay 2013; Patiri et al. 2012; Paz et al. 2013; Micheletti et al. 2014). The spatial and dynamical statistics of cosmic voids provide critical tests of structure formation and cosmological models (e.g. Peebles 2001; Benson et al. 2003; Park et al. 2012; Kolokotronis et al. 2002; Colberg et al. 2005b; Lavaux & Wandelt 2010; Biswas et al. 2010; Bos et al. 2012a; Park et al. 2012; Bos et al. 2012b; Hernández-Monteagudo & Smith 2013; Clampitt et al. 2013).

The voids in the galaxy distribution have been extensively studied and characterized by several authors in a variety of wavelengths (Pellegrini et al. 1989; Slezak et al. 1993; El-Ad & Piran 1997; El-Ad et al. 1997; Aikio & Mähönen 1998; El-Ad & Piran 2000; Müller et al. 2000; Arbabi-Bidgoli & Müller 2002; Plionis & Basilakos 2002; Hoyle & Vogeley 2002, 2004; Hoyle et al. 2005; Colberg et al. 2005b; Ceccarelli et al. 2006; Patiri et al. 2006; Shandarin et al. 2006; Platen et al. 2007; Brunino et al. 2007; Hahn et al. 2007; Neyrinck 2008; Foster & Nelson 2009; Lavaux & Wandelt 2010; Tavasoli et al. 2013; Elyiv et al. 2014) and show similar properties, even though a variety of identification methods and data samples are used (Colberg et al. 2008). Also, the void phenomenon has been a target of many theoretical analysis in numerical simulations (Hoffman & Shaham 1982; Hausman et al. 1983; Fillmore & Goldreich 1984; Icke 1984; Bertschinger 1985; Kauffmann & Fairall 1991; Padilla et al. 2005; Aragon-Calvo et al. 2010; Aragon-Calvo & Szalay 2013).

As voids expand, matter is squeezed in between them and the walls, filaments and clusters, generating the evolution void boundaries (Martel & Wasserman 1990; Regos & Geller 1991; Dubinski et al. 1993; van de Weygaert & van Kampen 1993; Bond et al. 1996; Goldberg et al. 2005; Padilla et al. 2005; Cautun et al. 2014).

⋆ e-mail: andresnicolas@oac.uncor.edu

Moreover, at early times the large-scale velocity field outflowing from underdense regions is associated with the linear collapse of overdense regions and shaped by the tidal influence of the surrounding mass distribution (Tidal Torque Theory Doroshkevich 1970; Peebles 1969; White 1984; Porciani et al. 2002b,a). This process imprints correlations between the inner dynamics of haloes and their host filaments and void distribution as well (Patiri et al. 2006; Paz et al. 2008; Paz et al. 2011; Schneider et al. 2012; Smargon et al. 2012; van Daalen et al. 2012; Zhang et al. 2013; Forero-Romero et al. 2014). However, this interplay is not only originated by the linear growth of initial fluctuations, but also affected by the vorticity of the cosmic velocity field which arises in the non linear phase (Pichon & Bernardeau 1999; Laigle et al. 2013; Wang et al. 2014). The antisymmetric component of the velocity deformation tensor also plays a major role in shaping the cosmic web, producing preferred directions for dark matter haloes and galaxies (Libeskind et al. 2014).

In previous works we examined the distribution of galaxies around voids in the Sloan Digital Sky Survey (SDSS) and performed a statistical study of the void phenomenon focussing on void environments (Ceccarelli et al. 2013, hereafter Paper I) and void dynamics (Paz et al. 2013, hereafter Paper II). To that end, we have examined the distribution of galaxies around voids in the SDSS by computing their redshift space density profile (Paper I), and recovering their underlying real space density and velocity profiles (Paper II). The real space profiles were inferred through modeling void-galaxy redshift space distortions on the two-point correlation function (Paper II). Sheth & van de Weygaert (2004) presented theoretical foundations that established a dynamical dichotomy of voids. According to the authors, there are two distinct void behaviours depending on their environment: the so called "void-in-void" and "void-in-cloud" process. The void-in-void regions are embedded in larger-scale underdensities and show expanding velocity profiles. On the other hand, void-in-cloud regions are surrounded by larger overdense environments which undergo in a former collapse, shrinking at later times the embedded void region. This last case seems to affect more likely small rather than large voids. The main goal of our previous studies was to confirm by the first time on observations this dynamical classification.

We defined in Paper I a separation criterion based on the redshift space integrated density profile to characterize voids according to their surrounding environment. Such criteria have shown success in separating expanding and contracting voids (Paper II) and allow us to define two characteristic void types: (i) voids with a density profile indicating an underdense region surrounded by an overdense shell, dubbed S-type voids, which behaves like a "void-in-cloud" process; and (ii) voids showing a continuously rising integrated density profiles, defined as R-type voids, which expand in a similar way as "void-in-void" regions. In this paper we analyse in detail the structure and dynamics of the velocity field in the regions surrounding voids. The aim of this work is to shed some light on the origin of the observed deviations of void velocity profiles from linear theory (Paper II), and address whether such deviations arise in the inner shell structure (i.e. the features of the density field inside shells) or they are more related with the surrounding large scale characteristics (i.e. void of interest classified as R or S-type). To this end we follow our previously defined classification scheme for void environments (R and S-types), where we analyse the velocity and density field inside void centric shells.

The organization of this paper is as follows. In Section 2 we describe the numerical N-body simulation used and the construction of the corresponding void catalogue. We describe the methods and present the results of the analysis of the dynamics of void shells in Section 3. In Subsection 3.1 we present the analysis of void shells on the basis of an equal area pixelization scheme, distinguishing pixels according to their local density. The kinematics of regions defined by the different sets of pixels are are analyzed in Section 3.2, where we use these sets to characterize the network structure and the stratum of low densitiy regions. A comparison of the structures defined by the different sets is made on the basis of the properties of minimal spanning trees on Sections 3.3 and 3.4. Finally, in Section 4 we present the conclusions of our results.

2 VOID CATALOGUE

2.1 The N-body simulation

In this work we use a dark matter simulation of 512^3 particles evolved from an initial redshift of $z \sim 50$ to the present time in a comoving box of side length $L = 500h^{-1}$Mpc. The cosmological parameters correspond to a flat ΛCDM model consistent with the WMAP7 estimations (Jarosik et al. 2011), with a matter density parameter $\Omega_{\rm m} = 1.0 - \Omega_\Lambda = 0.258$, a dimensionless Hubble constant $h = 0.719$ and a normalization parameter $\sigma_8 = 0.796$. The resulting mass particle is $m_{\rm p} = 6.67\times10^{10}h^{-1}{\rm M}_\odot$. The initial conditions were generated using GRAFIC2 (Bertschinger 2001) and the simulation was evolved using the public version of GADGET-2 (Springel 2005). The identification of haloes was performed using a Friends-of-Friends algorithm (Huchra & Geller 1982; Davis et al. 1985, hereafter FoF) with a percolation length given by $l = 0.2\,\bar{n}^{-1/3}$, being $\bar{n}$ the mean number density of dark matter particles. The final catalogue contains 505126 haloes with at least 10 particles.

2.2 Void identification

We perform the identification of voids using a modified version of the algorithm presented by Padilla et al. (2005) and Ceccarelli et al. (2006). The identification is done according to the following steps:

(i) Using the halo catalogue as structure tracer, we perform a Voronoi tessellation using the public library VORO++[1] (Rycroft 2009). This allow us to estimate the density field as the inverse of the Voronoi volume for each cell.

(ii) The candidates to underdense regions are selected at the centroid position for each cell with estimated overdensity satisfying $\delta < -0.8$.

(iii) Centred on each candidate position, we compute iteratively the integrated density contrast (Δ) inside spheres of increasing radius, denoted by r. When the integrated overdensity satisfy $\Delta(r) > -0.9$, the iteration ceases and the current sphere radius r is defined as the radius of the void candidate. If the threshold on $\Delta(r)$ is never achieved the candidate is not considered anymore as a possible void.

(iv) Once underdense regions are identified, the step (iii) is repeated starting this time from a randomly displaced center instead of the candidate centroid. Such displacement takes the form of a random jump proportional to the void radius. These random jumps are performed several times, obtaining a random walk around each candidate. Each jump is only accepted if the new obtained radius is larger than the last accepted value. If the current step is accepted, the candidate center is updated to the new position. The purpose of

[1] http://math.lbl.gov/voro++/

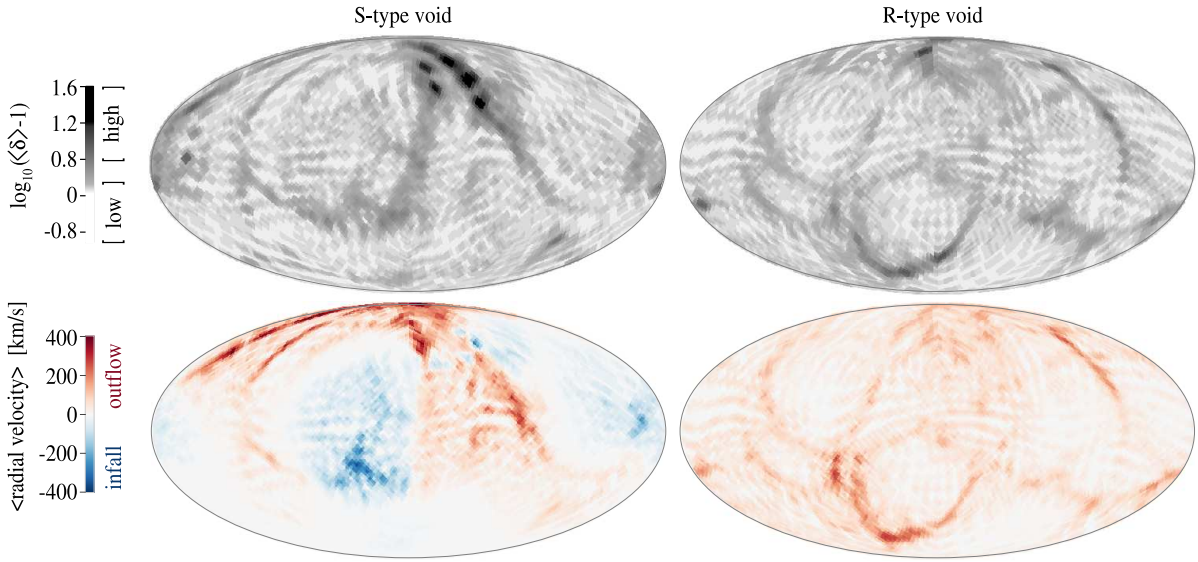

Figure 1. Mollweide projection of mass density contrast (top panels) and radial velocity (bottom panels) pixel maps of two voids with the utmost S ("void–in–cloud", left panels) or R-type ("void–in–void", right panels) behaviour. All simulation particles in the range $0.9 < r/R_{\rm void} < 1.1$ are used to compute averaged values within each pixel. The two voids shown in this Figure have been chosen so that they show the greatest separation in the void classification scheme, based on the integrated density profiles (detailed in Paper I). This two cases exemplify how the structure of the velocity field in the inner parts of a void at 1 void radius exhibits very distinct behaviour depending on their environment (defined around 3 void radius, i.e. R- or S-type void). Such differences are not expected in linear theory, given that both regions by definition enclose the same amount of integrated overdensity $\Delta(R_{\rm void}) = -0.9$.

such random walk is to recenter the identified voids in the largest scale local minimum of the density field. This procedure derive a well defined center which allows the computing of several stacking statistics like the correlation function or radial averages profiles (Ceccarelli et al. 2008).

(v) The last step consists on rejecting all the overlapping spheres, starting for the largest candidate.

As any void definition, the one presented in the above paragraph have some features which can be related by analogy to other identification algorithms. However in order to compare results among the literature corpus some caveats should be taken into account depending on the details of the void definition. For instance, several algorithms involve the construction of a hierarchy of voids, defined as regions enclosed by matter ridges (see for instance Colberg et al. 2005b; Platen et al. 2007; Neyrinck 2008; Elyiv et al. 2014, and references therein). In those cases, the value of the density field inside void regions could vary in a wide range. In our case we select voids by ensuring an enclosed density below a given threshold. For this reason, it is not straightforward to relate the underdense regions identified on both methodologies.

Following the procedure presented in Paper I, we have defined two types of voids depending on their integrated density contrast profiles. The mean of these profiles have been computed for different void size ($R_{\rm void}$) intervals. As shown in Paper I, such average curves have a well defined maximum at a distance $r_{\rm max}$ from the void centre, except for the largest voids which exhibit an asymptotically increasing profile. This radius typically reach void centric distances around $r_{\rm max} \approx 3R_{\rm void}$. Therefore the density at such scales can be thought as a measure of the large scale environment where the void is embedded.

We classify voids into two subsamples according to positive or negative values of the integrated density contrast at $r_{\rm max}$. Due to the linear theory, such definition implies that the region surrounding the void has negative or positive velocity divergence at those scales. This imply that this region is either in contraction or expansion, respectively. Voids surrounded by an overdense shell are dubbed S-type voids, and satisfy the criterion $\Delta(r_{\rm max}) > 0$. On the other hand R-type voids are defined as those that satisfy the condition $\Delta(r_{\rm max}) < 0$, which corresponds to voids with continuously rising integrated density profiles. More details about this void classification scheme can be found in Paper I and II. The simulation box is found to contain 1622 voids with sizes ranging from $\sim 9.5h^{-1}$Mpc to $\sim 29h^{-1}$Mpc, where 810 are S-type and 812 are R-type.

3 ANALYSIS OF THE STRUCTURE IN SPHERICAL VOID-CENTRIC SHELLS

In this Section we aim to investigate whether there is a relation between the spatial distribution, shapes and dynamics of structures surrounding voids, depending on its classification (i.e. R- or S-type void). As we summarized in the previous section and we have seen on Paper I and Paper II, this classification scheme successfully reflects the dichotomy on the dynamics of underdense regions. The linear theory predicts the future collapse and expansion of S- and R-type voids, respectively. The theory also predicts that the behaviour in the inner parts of an underdense region is insensitive to whether it is surrounded by any kind of environment (i.e., S- or R-type): the velocity profile only depends on the amount of enclosed mass. However in Paper II, we have seen significant deviations from the linear predictions in the inner parts of void velocities profiles, both in R- and S-type voids (see Figure 3, in Paper II). Similar qualitative results can be found in the work of Hamaus et al. (2014a), who found deviations from the predicted radial velocity profiles of stacked voids in the inner regions (around 0.5 to 1 void radii), being these differences more relevant for small voids. Nonetheless, only a qualitative comparison between our results and those in Hamaus

et al. (2014a) is possible, due to differences on the void definition and identification algorithms. Voids used in their work are identified accordingly to a hierarchy (Neyrinck 2008), where small underdense regions can be found inside of larger voids with a higher cumulative mass overdensity. In consequence, there are differences between definitions of void radius and center. At the same time, their results are not classified into S- or R-types and therefore their stacked profiles reflect the two dynamical behaviours (specially for small sized voids).

At first glance, it could be conjectured that inner parts of underdense regions quickly reaches the lower bounds of the validity domain of the linear theory (i.e. nonlinear dynamics becomes increasingly significant as δ approaches to -1). However, the purpose of this Section is to get a deeper insight on the issue, by attempting to derive the specific source of such discrepancies from linear theory. To this end, we analyze the properties of different tracers used to map the void velocity field. The properties taken into account involve local density, shapes, and spatial distribution of matter around voids.

We consider spherical shells of various sizes centered on each void in the sample. In all cases the radial width of a given shell is a 20 per cent of the void radius. For each void, the smaller shell is centered at $r = R_{\rm void}$ and the larger one at a distance of $r = 3R_{\rm void}$. The shells are spherically tessellated with equal area pixels computed using the software HEALPix (Górski et al. 2005). We need a pixelization scheme where pixels are not too large, in order to resolve the shapes of structures conveniently. However, the shot noise increases when the size of the pixels drops down, since most of the pixels contain no particles. We use a pixelization scheme with 5 levels of refinement ($N_{\rm side} = 32$) giving a total of $N_{\rm pix} = 12\ N_{\rm side}^2 = 12288$ pixels for each map. The results shown in this work do not depend on the resolution of the pixelization scheme.

3.1 Velocity and density angular distribution

We applied the described shell tessellation scheme to all voids in the simulation box (Sec. 2.2) and computed the density and mean radial velocity of particles on each pixel of a given shell ($\rho_{\rm pix}$ y $V_{\rm pix}$). Since this pixelization is performed on an equal area basis, the density is simply proportional to the number count of particles in a pixel, at a distance within the limits defined for each shell. In order to study the dynamics of structures in an expanding/collapsing void scenario (as discussed in Paper II) we computed the averaged void–centric radial velocities of the particles per pixel and per void. Examples of the pixelized maps of density contrast and radial velocity corresponding to a shell located at $r = R_{\rm void}$, are shown in Mollweide projection in Figure 1. Left panels show the maps for a S-type void, and right panels correspond to a case of a R-type void. We selected the S-type (R-type) void with the maximum (minimum) value of integrated density profile at $r_{\rm max}$ of the void sample (as defined in section 2.2), so that they exhibit the utmost R- and S-type behaviours. This selection of the utmost R- and S-type void behaviours has been carried out in 6 void subsamples in voids size intervals of $3h^{-1}$Mpc (see Figure 2). For simplicity, in Figure 1 we only show the results for one of these void subsamples. The upper panels show the logarithmic density contrast of the mass $\log_{10}(\delta_{\rm pix} + 1) = \log_{10}(\rho_{\rm pix}/\bar{\rho})$, where $\bar{\rho}$ is the mean density of the simulation. In the bottom are the radial velocity maps, showing the infalling and expanding regions. The grid patterns seen in low density regions are due to the relatively small size of the pixelization scheme chosen, and arise as a result of the simulation grid. However, the selected map resolution results adequate to analyse structures at high density regions. By definition of the void identification method, both void shells at $r = R_{\rm void}$, enclose the same amount of integrated density contrast $\Delta(R_{\rm void}) = -0.9$. Even more, both voids have similar sizes, 12.6 and 15.1 h^{-1}Mpc for S- and R-type void respectively.

The motions of shells enclosing an overdense or underdense sphere arise naturally as a consequence of the gravitational pull and is predicted in its simplest form by the linear theory (Peebles 1976). According to this, in a standard ΛCDM model, the radial velocity of a shell at radius r enclosing an integrated mass overdensity $\Delta_{\rm m}$ is given by:

$$V_{\rm lin}(r) = -\frac{H}{3} r \Delta_{\rm m}(r) \Omega_{\rm m}^{0.6}, \tag{1}$$

where H is the Hubble parameter and Ω_m is the cosmological dark matter density parameter. At first glance, by Eq. (1) we roughly expect the same behavior of the mean radial velocities for the two cases shown at Figure 1 (i.e. by definition both enclose almost the same amount of matter density). However, as it can be seen in the lower panels of Figure 1, the fluctuations of the velocity field around this mean velocity behaves notably different. In the S-type shell there are regions with net infall (blue pixels) or outflow velocities (red pixels). In contrast, for the R-type spherical shell we only observe positive radial velocities (i.e., outflow). Also, by comparing bottom to top panels it can be seen that the regions with a defined sign in radial velocity (i.e. outflow or infall) seem to correlate with projected structures in the density map. We have found similar features in all of the 6 void size subsamples mentioned above. Even though, we should emphasize that the maps shown in Figure 1 are not the typical behaviour of S- and R-type voids. As stated above, they are just representative of voids with the largest environment differences. Since our void classification scheme is based only on two categories, there are plenty of voids with density profiles which fall into a grey area between both cases. However, guided by the insights obtained here, in the following Sections we will perform a statistical analysis intended to characterize the features of the angular velocity/density field in void centric spherical shells.

In order to complement the discussion based on Figure 1, we also analyse the utmost R- and S-type voids (as defined previously) in six void size ranges. For this purpose, in Figure 2 we plot the histograms of the pixel averaged radial velocity for these voids, showing S-type in black solid lines and R-type in black dashed lines. The results for different sizes are shown on each panel as indicated in the top-right labels. Grey curves display the corresponding histograms for all voids in a given size range. As it can be seen, in all cases the utmost R-type voids present a narrow velocity distribution with a well defined peak, and with almost all the pixels with a positive radial velocity (i.e. outflow behaviour). In contrast, the utmost S-type voids show wider distributions and in a variety of shapes, covering from flat to multi peak distributions, and with a large component of infalling pixels (i.e. negative radial velocity). As can be seen, the velocity histograms for all voids seem to be enclosed by the velocity distribution of the extreme R- and S-type voids. This indicates that the selection of utmost behaviours based on its density profiles is also manifested in the fluctuation of the velocity field in the inner parts of voids (the shell is located at $r = R_{\rm void}$). For the last size interval (largest voids, lower-right panel), S- and R-type voids show similar distributions. This is expected because larger voids tends to have an R-type behaviour and the fraction of S-type voids decrease (see Paper I for details).

The results presented in this subsection suggest a systematic correlation between the fluctuations of the velocity field at the inner

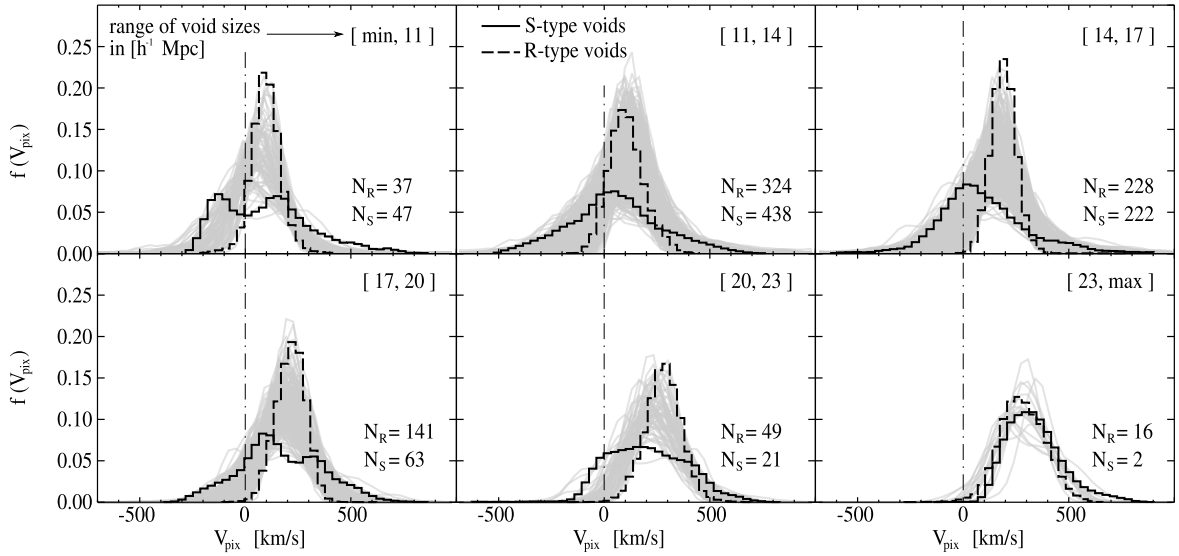

Figure 2. Normalized histograms of pixel radial velocities for the S-type (black solid lines) and R-type voids (black dashed lines) with the largest differences in their radial profiles (i.e. the S-type void with the largest density around $3R_{\rm void}$ and the R-type void with the lower density at the equivalent scale), selected in six void size intervals of width $3h^{-1}$Mpc, except the first and the last ones. Grey curves correspond to all the voids in that size range. The dot-dashed line marks the position for $V_{\rm pix} = 0$, the transition from outflow to infall behaviour. The void size increases from top to bottom and from left to right, as indicated in the top-right label of each panel. The number of voids with R or S type environments (N_R and N_S) are indicated at the left bottom legends.

parts of voids (i.e. $r = R_{\rm void}$, where the integrated density is around $\Delta = -0.9$) and the void environment at large scales ($r \sim 3R_{\rm void}$). As discussed at the beginning of this Section, these correlations can shed some light on the origin of nonlinearities in the inner parts of the underdense regions. This kind of systematic deviations in the velocity field may have in principle some impact on studies using void-galaxy redshift space statistics (Lavaux & Wandelt 2010; Paz et al. 2013; Hamaus et al. 2014b). The fact that the regions of infall or outflow on the utmost S-type voids seem to be clustered in angular positions (see left-lower panel in Figure 1), indicates that it may be a correlation between the velocity deviations around the mean flow and the properties of the large scale structures. Inspired on these features, in the following sections (3.2 and 3.4) we will analyse the dependence of the velocity field on the density and shape of the surrounding structures.

3.2 Dynamics of low and high density regions in void shells

As described in the previous section, for each void we compute angular maps of radial velocity and density in spherical void centric shells of varying radii. Shell radii span a range between 1 and 3 times the void radius. We divided the full set of pixels in each shell into three categories according to its density contrast with respect to the mean density of the simulation ($\delta_{\rm pix}$): low density regions are defined by pixels with $\delta_{\rm pix} < 1$, intermediate density regions satisfy $1 < \delta_{\rm pix} < 5$ and high density regions are selected with $\delta_{\rm pix} > 5$. Such selection is intended to separate high and low density structures from the stratum of mass with an average behaviour. For each shell we obtain the average radial velocity (denoted by $\langle V_r \rangle_{\rm shell}$) by computing the average of pixel radial velocities in one of the three density subsets defined above. This allows to roughly estimate whether structures of a given density are moving away from or falling into the void center (i.e. the shell pixel subset of a given density have a net expansion or contraction). Finally, following Eq. (1), we calculate the linear prediction of radial velocities, $V_{\rm lin}$, for all voids at the different shells.

In Figure 3 we show the distributions of these average velocities as a function of the shell radius normalized to the void radius. These distributions represent the joint probability density of shells and were estimated by simply counting high or low density shells in bins of r and $\langle V_r \rangle_{\rm shell}$. Since by definition we have two velocity averages (high and low density pixel subsets) at all shell radii for each void, the sampling in shell sizes is homogeneous. This allows to directly compare between the results corresponding to each subset centered rather on R- or S-type voids, and also to perform comparisons between both void categories. Solid lines in Figure 3 show isopercentile curves of the distribution corresponding to the subset of low density pixels, whereas shaded regions indicate the same percentiles for the subset of high density pixels. The inner curves/regions represent the 40 per cent of the sample and the outer ones the 90 per cent. The dotted central line corresponds to the median of the distribution of the linear model prediction. The top and bottom panels show the results for shells centered on R- and S-type voids, respectively. On the right-hand side of Figure we display histograms of radial velocities for two intervals of radial distance: a shell centered at one void radius and a shell at 2.5 void radius. Finally, the vertical dotted line indicates the position of $\langle V_r \rangle_{\rm shell} = 0$ in the histograms.

It is worth noticing that in Figure 3 the mean radial velocity distributions for all cases (R- or S-type voids with high or low density pixels) qualitatively follow the behaviour of the linear theory prediction. In all cases this model is enclosed within the central 40 per cent of the distributions. This is consistent with the previous results reported on Paper II, where we showed that linear theory can be used to model redshift distortions around voids. In the same direction, S-type voids exhibit typical negative velocities at large shell radius (around 1.5 to 3 void sizes). This is the typical behaviour of "void-in-cloud" regions described by Sheth & van de Weygaert (2004) and observed on the SDSS (Paper II). On the other hand, by looking at the top panel of Figure 3 (S-type voids), it can be seen that the velocity distribution of low density pixels is nearly symmetric around the linear theory median prediction. In contrast,

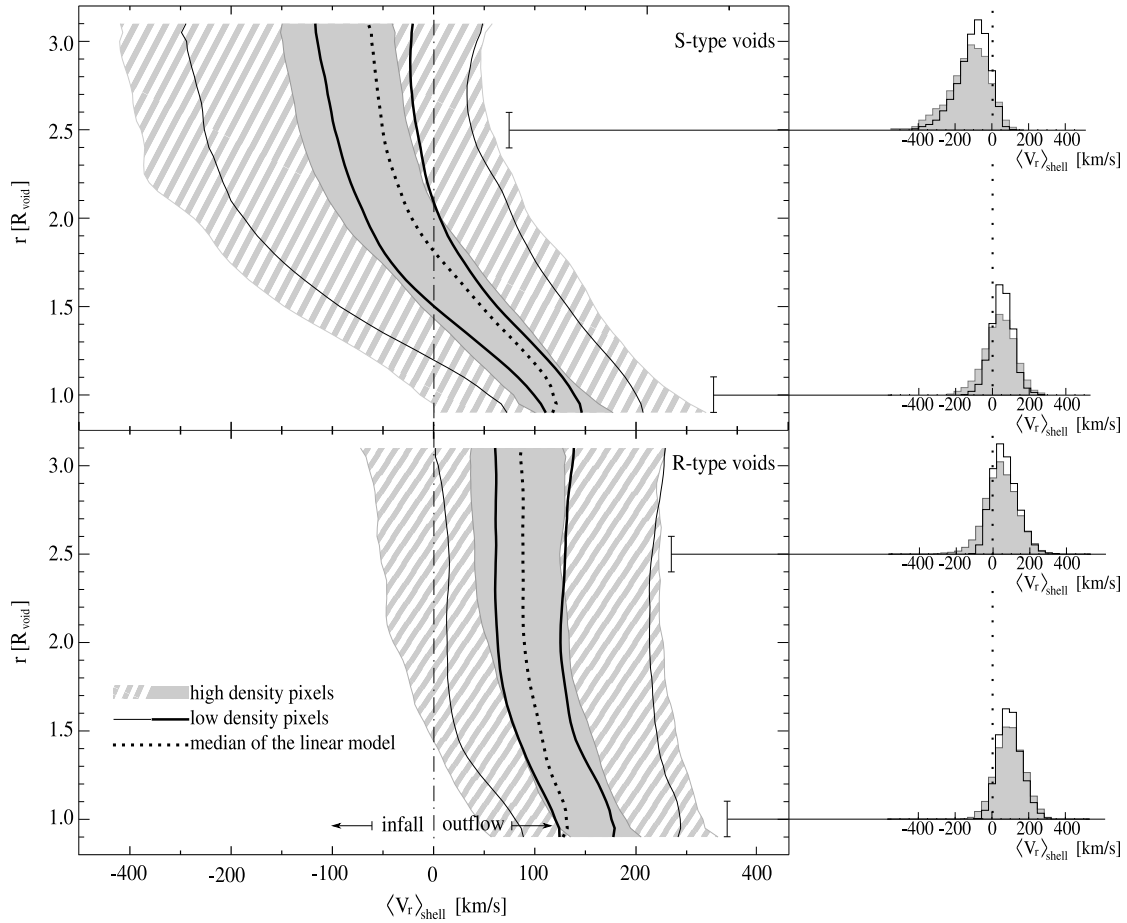

Figure 3. Joint probability density distribution of shell mean radial velocity $\langle V_r \rangle_{\rm shell}$, and the shell radius r (in void size units $R_{\rm void}$), for S-type (top panel) and R-type (bottom panel) voids. Solid lines show isopercentiles of the distribution of low density pixels and shaded regions show the same percentiles corresponding to network structures, formed by high density pixels. Inner curves/regions represent the 40 per cent of the sample and the outer ones the 90 per cent. The dotted central line corresponds to the median of the linear model prediction given by Eq. (1) and the dot-dashed line marks the position of $\langle V_r \rangle_{\rm shell} = 0$, i.e. the infall/outflow transition. Plots on the right-hand side of Figure show the normalized histograms of radial velocities for two intervals of radial distance: a shell at nearly one void radius and a shell at roughly 2.5 void radius. The dotted line that crosses the histograms indicates the position of $\langle V_r \rangle_{\rm shell} = 0$.

high density pixels exhibit a shift towards greater infall velocities with respect to the median linear theory. Also the outer contours (which enclose the 90 per cent of the population) indicate a broader distribution of velocities at these densities. This suggests that the larger deviations from linear theory observed on S-type voids (Paper II) are mainly reflected in the dynamics of the surrounding high density peaks. However, we should emphasize that the deviations described here are around the median linear theory values. These deviations are source of dispersion and errors in stacking statistics as those presented in Paper II, where the dynamics of a given void sample is modeled by applying linear theory to the mean or median density profile. Studies using a mixture of S- and R- type voids (see for instance Hamaus et al. 2014a), have also report systematics deviations from linear theory, in qualitative agreement with our results. For the case of R-type voids (bottom panel), it is worth noticing that more than 90 per cent (outer contours) of low density pixel averages distributes only over positive velocities. According to the "void-in-void" dynamics, this type of voids should only display expansion velocity curves. However, the high density pixels show a significant fraction of structures with net infall averaged velocities. Here again the high density peaks at distances ranging from ~ 1.5 to ~ 3 void radius are the main responsible for the deviations from linear theory.

We have analysed deviations of the velocity field from the median of linear theory predictions depending on the density of the pixel and the type of the void centre. In order to see whether such deviations relies in the first order approximation of linear theory, we study the distribution of radial velocity in void shells relative to its corresponding linear prediction. To this end, for each shell and pixel density subset, we compute the difference between the mean radial velocity and the value expected from linear theory (i.e. $\langle V_r \rangle_{\rm shell} - V_{\rm lin}$). Looking for a more quantitative analysis, for all distributions we compute four moments: the first and second moments (mean and standard deviation) plus third and fourth standardized moments (skewness and kurtosis). The results are shown in Figure 4, where S-type voids are indicated with solid lines whereas R-type voids are drawn with dashed lines. The thickness indicates low and high density regions for thin and thick lines, respectively. The first three panels from up to bottom correspond to the mean, standard deviation and skewness, whereas the kurtosis is not show because it is statistically consistent with zero at all radii. In the panel (d) , we show the skewness of the distributions of $\langle V_r \rangle_{\rm shell}$. As can be

seen, the results shown in this panel are consistent with distributions displayed in Figure 3. The S-type void velocity distributions show asymmetry toward infall velocities (negative skewness) for both high and low density regions. Such asymmetry could arise from the systematic collapse of the surrounding void region. When the linear velocity is subtracted (panel (c)), the skewness of the distributions vanishes or diminishes considerably. This indicates that the deviations from gaussianity in the velocity distributions can be explained mostly by means of linear theory. On the other hand, R-type voids exhibit marginally positive skewness in its velocity distribution (panel (d) in Figure 4), which is consistent with the observed suppression of negative velocities in Figure 3. Respecting to the mean of velocity deviations (panel (a) in Figure 4), S-type voids show larger deviations from linear theory than R-type voids, along the whole scale range. Among S-type voids, the largest deviations are present when using high density regions to compute radial velocities. However at shell radii below 1.5 void sizes, R-type voids also present important deviations from linear theory values. These results suggest that low density tracers for S-type voids and high density tracers for R-type voids are more likely to reproduce linear theory predictions. This can be important in studies that depend sensitively on the modeling of the velocity field surrounding voids. As an example, it could be mentioned works intended to perform the Alcock-Paczynski test (Lavaux & Wandelt 2012; Sutter et al. 2012) on voids identified on sparse galaxy samples, which are expected to be dominated by R-type voids (Paper I) and high luminosity tracers. These studies are sensible to anisotropies induced by redshift space distortions (Paper II), and therefore a proper modeling of the velocity field is required. In the same direction, studies based on low redshift samples, as the main galaxy sample of the SDSS, can be benefited by an appropriate treatment of the velocity tracer population. The last rely in the fact that such samples are expected to be dominated by S-type at small size voids whereas at larger size R-type voids become more frequent (Paper I).

Finally, in Figure 5 we show the median of $\langle V_{\rm r}\rangle_{\rm shell}$ normalized to the linear prediction $V_{\rm lin}$ as a function of the void size $R_{\rm void}$ for S-type voids (top-left panel, solid lines) and R-type voids (top-right panel, dashed lines). These values correspond to the shell located at a distance of one void radius from the center. The values for high density pixels are plotted in thick lines and the low density regions are shown whit thin lines. It is clear from this Figure that there is a dependence of the mean radial velocity of the shell on the void size, in both types and densities. This dependence is more pronounced for S-type voids, and the high density regions have more dispersion than the low ones. The normalization with the linear model ensures that this correlation is a feature beyond the linear dependence with size present in Eq. (1). The values of the median radial velocity for S-type voids are underpredicted by a $\sim$ 10 per cent in the median with respect to the linear theory for small voids (and more evident for the high density pixels) and overpredicted by a $\sim$ 20 per cent in the median for the larger voids in our sample. For the sample of R-type voids we note an overprediction from $\sim$ 10 to $\sim$ 20 per cent in the median in all the sizes range. At the bottom panel of Figure 5 we show the median of the cumulative mass overdensity inside the shell located at $R_{\rm void}$ as a function of the void radius for the whole sample, irrespective of the void environment. As can be seen, there is a trend with the void radius which can be used to explain the increasing deviations from linear theory with void size. That is, larger voids tend to have more non-linear values of cumulative mass overdensity, which as a result make the dynamic of these voids less described by the linear theory. However, the differences between the deviations when comparing R- and S-type voids are

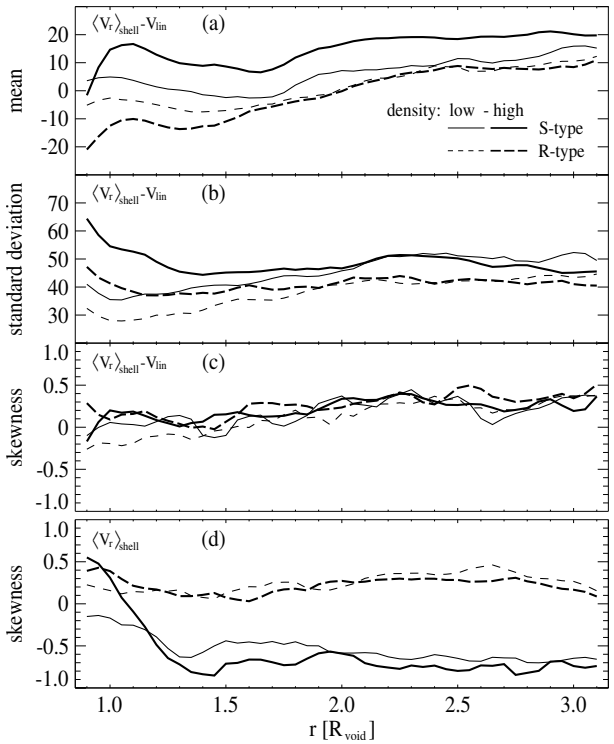

Figure 4. Moments of the distributions of radial velocity relative to the linear prediction ($\langle V_r\rangle_{\rm shell} - V_{\rm lin}$) as a function of the void–centric distance (three first panels from up to bottom). S-type voids are indicated with solid lines and R-type voids with dashed lines. The high density regions are plotted with the thick lines and the low density ones with thin lines. In the fourth panel (bottom), it is displayed the third standardized moment (skewness) for the same distributions of radial velocities of Figure 3.

notably different. This result becomes more relevant if we notice that the behaviour of the cumulative overdensity with void size have negligible difference for both R- and S-type voids (the corresponding curves can not be seen due to the fact that they lie inside the grey shaded area in the bottom panel of Figure 5). Therefore, even when the discrepancies with linear theory are mostly explained by the emptiness of the inner parts of underdense regions, they exhibit a notably different behaviour depending on the large scale environment.

3.3 Structures in the high density regions

Once pixels have been classified according to its particle density contained within the spherical shell, we can separate them in density intervals in order to study their properties. The selected pixels in a density layer form clustered regions or "chunks", which represent the projection of structures surrounding the void within a spherical slice of a given size. These structures appear in a rich variety of shapes and complexity, which depend on the density of their constituent pixels, the distance to the void centre and the dynamics of the corresponding void. We argue that these dependences encode useful information about the large–scale structure of the void–filament network, and also possibly about their formation and dynamics. We aim to study the morphological properties of the pixel structures in order to seek for and quantify such dependencies. As a first step, we isolated the structures by forming groups of adjacent or near pixels in the same density range. This can be achieved by applying a FoF percolation algorithm to the set

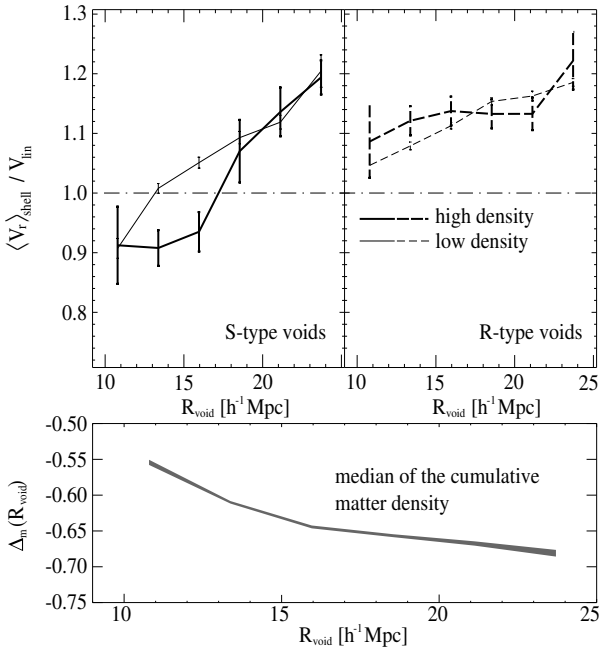

Figure 5. Median of the averaged radial velocities of each void relative to the linear prediction as a function of the void radius for S-type (upper-left, solid lines) and R-type (upper-right, dashed lines) voids. The thick lines correspond to the high density pixels and the thin lines to the low density regions. Errorbars show the standard deviations. The lower panel shows the median of the cumulative mass overdensity. The dot-dashed horizontal line indicates the prediction for radial velocities according to the linear theory. All panels refers to the shells located at $r = R_{\rm void}$.

of pixels, with an angular linking length equal to the mean pixel separation for the complete void sample divided by the void radius. The mean separation is around to $\sim 3h^{-1}$Mpc for the case of the densest pixels. This procedure leads to a number of pixel groups with a diversity of arrangements, from compact to multibranch filamentary or "spider like" structures. A number of strategies could be used in order to quantify the geometry of the arrangements of pixels. The simplest method to characterize their forms is possibly the computation of a normalized inertia tensor to obtain the elongation as the ratio of the minor–to–major axes. The semi–axis method has been used to characterize both 3D and 2D structures (Babul & Starkman 1992; Luo & Vishniac 1995; Sathyaprakash et al. 1998; Paz et al. 2006, and references therein). This procedure, however, does not distinguish between different levels of compactness or filamentarity. Other approaches have been proposed to characterize the geometry of complex structures, most notably Minkowsky functionals (Bharadwaj et al. 2000; Basilakos 2003; Einasto et al. 2007; Costa-Duarte et al. 2011), surface modeling via triangulated networks (Sheth et al. 2003) and shapefinders of several kinds (e.g. Sahni et al. 1998; Aragón-Calvo et al. 2007).

We find useful to represent the set of pixels in a group by a two-dimensional graph, where each node is a pixel and any pair of nodes is connected by an edge with a weight equal to the angular distance between the centers of the pixels corresponding to the adjacent nodes. The disposition of nodes and the general geometry can be easily computed by means of the minimal spanning tree of the graph (Barrow et al. 1985, hereafter MST), defined as the shortest weighted path that connects all the nodes without cycles. This tree can be constructed for a set of pixels with the Kruskal algorithm (Kruskal 1956), using the positions of pixels and the spherical distances between them. An important MST characteristic is its length L, equal to the sum of the weights of all its edges. The maximum distance between any pair of nodes, $D_{\rm max}$, is also a useful quantity, which combined to the length allows to define an estimator of structure elongation, $E = D_{\rm max}/L$. This last parameter is dimensionless and by construction its value ranges between 0 and 1, where groups with an elongation value of roughly 1 are filaments or thread–like structures, and groups with a low elongation value are compact or concentrated structures.

We compute the maximum separation, length and elongation estimators for all structures arising from pixels in the high density layer, once again as in previous subsections, in a shell centered at $r = R_{\rm void}$. As we discussed in section 3.1, we are interested in characterizing in a statistically robust basis, the deviations from linear theory in the angular structure around voids, and whether they are related or not with the void large scale environment (i.e. R- or S-type void).

In Figure 6 we show the median values (black lines) and the standard deviation (grey lines) of MST parameters as a function of the void radius. S-type voids are drawn in solid lines and R-type voids in dashed lines. In the top panel we show the angular size of the MST length (L) and the maximum separation ($D_{\rm max}$), and in the middle panel the elongation parameter $E = D_{\rm max}/L$. As it can be seen in this Figure, these parameters do not depend significantly on void size, indicating that the definition of these quantities is not biased by the spatial size of the void shell. In order have a visual insight on the structure shapes and the elongation values, we show in the lower panel an example of the distribution of structures and their elongation parameters in a void shell.

In the next Section we use these parameters to explore the dynamics of structures depending on the void classification and size.

3.4 Dynamics of structures

Since the mass in the shells around voids is arranged in structures, specially when density levels are considered, the study of the velocities of these structures merits further investigation. In Section 3.3 we described the procedure to characterize the shapes of groups of pixels, as a proxy to the projection of structures within the shell, by means of the minimal spanning tree. This approach has a number of advantages, mainly its simplicity and the ability to differentiate between filamentary structures with several degrees of complexity.

In this Section we aim to characterize the smoothness of the radial flow of structures. To do this, we compute the averaged void–centric radial velocities, $\langle V_{\rm r}\rangle_{\rm str}$, and the averaged tangential velocities, $\langle V_{\rm t}\rangle_{\rm str}$, of all the structures resulting from the FoF percolation of high density pixels on each shell. The smoothness of the radial flow can be quantified by measuring the median of the ratio of radial to tangential velocities, namely $\langle V_{\rm r}\rangle_{\rm str} / \langle V_{\rm t}\rangle_{\rm str}$.

In Figure 7 we show the results of $\langle V_{\rm r}\rangle_{\rm str}$, $\langle V_{\rm t}\rangle_{\rm str}$ and $\langle V_{\rm r}\rangle_{\rm str} / \langle V_{\rm t}\rangle_{\rm str}$ as function of void radius considering separately S- and R-type voids. It can be seen that the radial flow smoothness of structures in void shells increases with void radius so that the largest the voids, the more significant the outward void–centric radial velocity as compared to their tangential motions. We find structures in R-type voids to have systematically smoother radial outflows compared to structures in S-type voids, and that radial flows dominate the dynamics for voids larger than $\sim 18h^{-1}$Mpc. Besides, it can be seen in the lower panels that this behavior is caused by the combined effect of structures in S-types to have a systematically lower radial flow and larger tangential motions. These results could be useful when modeling the velocity field in voids. For instance,

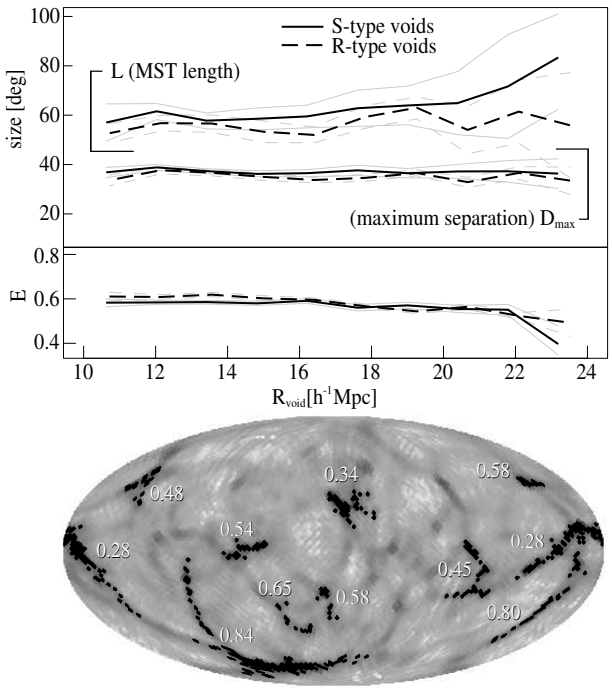

Figure 6. Shape parameters of structures within the shells centered at $R_{\rm void}$, of S-type (solid lines) and R-type (dashed lines) voids. Median values are shown in black and the corresponding errors in grey. In the upper panel we show the minimal spanning tree length (L) and the maximum separation ($D_{\rm max}$). In the middle panel, the median of the elongation values $E = D_{\rm max}/L$ are given as a function of void radius. In the lower panel we show an example of the angular distribution of structures and their corresponding elongation parameter values.

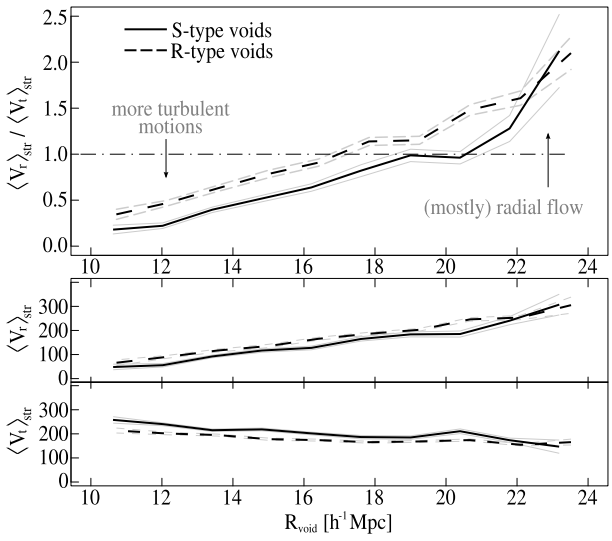

Figure 7. Median of the mean radial (middle panel) and tangential (bottom panel) velocities, in km/s, of structures of S-type (solid lines) and R-type (dashes lines) voids, as function of void radius. On the upper panel we show the ratio of radial-to-tangential velocity, which gives an estimate of the mass flow *smoothness*. Grey lines indicate the errors of the medians. The dot-dashed line mark the transition from more turbulent motions to a radial flow.

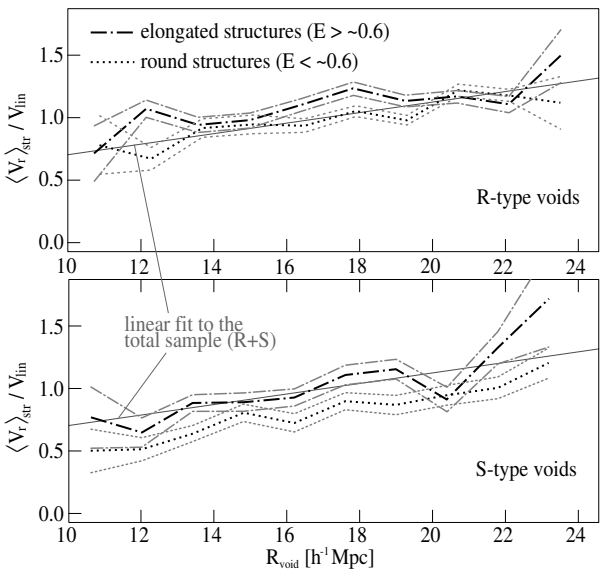

Figure 8. Median of the mean radial velocities of structures of each void relative to the linear prediction of Eq. (1) for R-type (upper panel) and S-type voids (lower panel) as function of void size. The samples has been divided into elongated (dot-dashed lines) and round structures (dotted lines), as described in the text. The trend for the whole sample (without separating in elongation or void type) is showed with the thin solid line. Grey lines correspond to the standard deviation.

in the case of measurements in redshift space (either correlation or stacking statistics), for certain void sizes, the results would be more affected by uncertainties in the pair-wise velocity dispersion than in the mean flow velocity. This could be inferred from the mentioned above dominance of tangential velocities on voids with radius below $18h^{-1}$Mpc. This is also the case for S-type voids at all sizes: they seems to be more affected by tangential velocities than R-type regions.

We have additionally explored the behavior of the mean radial velocities of structures relative to the linear prediction of Eq. (1) as function of $R_{\rm void}$. The results are given in Figure 8 where we have considered separately the sample of structures identified in R-type (upper panel) and S-type voids (lower panel), and each of this subsamples into elongated (dot-dashed lines) and round (dotted lines) structures. This last separation was performed according to the results of the middle panel of Figure 6: structures with elongation values higher than the mean ($E >\sim 0.6$) are considered as elongated, and structures with lower values as round. The solid thin line represents the global trend of the whole sample (a linear fit to the total void sample), with no shape restrictions. It can be seen that for both R- and S-type voids, the linear prediction provides an overestimation of the radial velocity of about $\sim$ 20 per cent in the median for small voids and an underestimation of $\sim$ 20 per cent in the median for the larger voids. The global behaviour for S-type voids in Figure 6 agree with the trend shown in the left panel of Figure 5. However, for R-type voids we note a discrepancy since the radial motion of shells is always underestimated by the linear model (see right panel of Figure 5), while structures identified in the high density pixels present the same velocity trend than structures in S-type voids. Depict this qualitative similar behaviours in both Figures (8 and 5), it should be emphasized that the quantities shown on each case have a different meaning. For instance, results on Figure 5 can be thought as the typical error obtained when the mean velocity of a given shell is predicted by linear theory. Mean-

while, in Figure 8, the displayed trend indicate the typical difference observed between the actual velocity of a given structure with the mean predicted by the linear model.

4 CONCLUSIONS

Based on the dynamical dichotomy first predicted by Sheth & van de Weygaert (2004), and confirmed on observations in previous works (Paper I, Paper II), we have explored the interplay between the inner dynamics of voids and its large scale environment. The presented study goes beyond our previous analysis, that examined the mean velocity profile of voids, here we have studied the velocity field structure (higher moments, angular distribution, etc.) in shells around them. The aim of this analysis was not only to inquire the existence of correlations between the inner void dynamics and its environment, but also was to look for clues on the origin of the nonlinearities (Paper II, Hamaus et al. 2014a) in the velocity field of voids.

We have analysed voids in different dynamical regimes, according to the R/S type classification presented in Paper I. In order to accomplish this, we have considered spherical shells around voids at several void–centric distances, analysing the transition between the domains of voids and surrounding structures. An statistical study on the spatial and velocity distributions on void-centric shells shows notably differences between void types and sizes. At the inner parts of the utmost S-type voids, the velocity distribution takes the form of angular patches with predominant infall or outflow radial velocities, even though the mean velocity in all cases is outwards. Meanwhile, for R-type voids, the velocity angular distribution is consistent with a pure outflow pattern. As a result, the distributions of deviations from the bulk flow on R-type voids are typically narrow, well centered on its mean values. In contrast, S-type voids typical exhibits an inner broad distribution of radial velocities, without a neat bulk flow peak or, in some cases, incipient bimodality. It should be noticed that between both utmost behaviours there is a continuous range of velocity patterns.

In the analysis for the radial velocity field at shells in increasing radii we find that R-type voids the velocity field remains with positive outflow at different shell radii, which contrast with the behaviour of S-type voids that show a significant infall beyond 1.5 void radii, in agreement with Paper II. The spread of void–centric radial velocities for S-type voids is significantly larger than that of R-type voids, particularly at large distances from the center. We also found that the distribution of velocities of the high density regions exhibit an infalling tail, which is remarkable for S-type voids but also notably on R-type voids. The linear model provides a suitable fit to the observed radial infall/outflow; however, in S-type voids, there is a systematic offset towards smaller values by approximately $\sim 30 - 50$ km/s. We have also seen that linear theory successfully predicts Gaussian deviations on radial velocity fluctuations (i.e. skewness and kurtosis moments are negligible on linear theory deviations). The results summarized in the above paragraphs, could be important when modeling the pair-wise velocity function on redshift space measurements and models (see for instance Paper II).

The ability of the linear theory is also tested when comparing the ratio of the observed radial velocity to the predicted one in the shell located the void radius, founding that this ratio is an increasing function of the void size for both S- and R-type and high and low density regions. An explication of this trend can be found by analysing the cumulative mass overdensity inside the shell, $\Delta_{\rm m}(R_{\rm void})$. As expected, larger voids have stronger non linear values of mass density, therefore the dynamics of larger voids are less described by a linear approximation (in agreement for instance with Hamaus et al. 2014a, and references therein). However, it is important to note that although the values of $\Delta_{\rm m}$ are indistinguishable between both S- and R-type voids, the trend of radial velocity with void size observed presents notably differences depending of the large scale environment. These results reinforce the idea repeated along this work: the nonlinearties observed in the inner parts of voids could arise from a coupling of scales. Large scale environment defined arround $3R_{\rm void}$ has a significant correlation with dynamics at inner scales ($-0.8 < \Delta_{\rm m} < -0.6$).

The structures defined in the high density regions of void shells provide further dynamical studies. We find that these structures shown similar deviations from linear theory than previous results, that is larger departures are seen at larger sizes. We found again that velocities traced by structures in both S- and R-type have a common transition scale, from linear model overprediction to underprediction, at void sizes around $\sim 18h^{-1}$Mpc. Besides, elongated structures exhibit systematically larger $\langle V_{\rm r}\rangle_{\rm str}/V_{\rm lin}$ values with respect to the rounder structures by ~ 20 per cent in the median. We have analysed the radial to tangential velocity ratio of the structures as a suitable measure of the void-centric flow smoothness. The results of this study show an increasing trend of radial flow smoothness as a function of void size produced by a systematically increasing mean radial velocity and a continuously decreasing tangential velocity. The observed correlation suggests that large voids (with sizes greater than $R_{\rm void} \sim 18h^{-1}$Mpc) have more frequently boundaries with structures dominated by radial outflows, in contrast with a more turbulent motion of the structures at boundaries of small voids. We also find structures in R-type voids to have systematically smoother radial outflows by ~ 25 per cent in the median compared to structures in S-type voids.

As a final remark, is worth to notice that R-type voids with larger sizes are the regions best described by linear theory and dominated by radial outflows. In addition, low density structures seem to trace the inner velocity field in better agreement with linear theory. This could be important when designing cosmological tests based on voids samples and the oncoming next generation of large volume galaxy surveys as HETDEX (Hill et al. 2008), Euclid (Laureijs et al. 2011), SDSS-III (Eisenstein et al. 2011) and VIPER (Micheletti et al. 2014). In particular measurements which depends on a proper modeling of the velocity or density void profiles (e.g. the Alcock-Paczynski test or the Integrated Sachs-Wolfe effect, Granett et al. 2008; Pápai et al. 2011; Lavaux & Wandelt 2012; Sutter et al. 2012; Hernández-Monteagudo & Smith 2013; Ilić et al. 2013; Cai et al. 2014b,a). For these next generation surveys, given the large volume sampled, it is expected to identify voids by using high luminosity tracers. Voids catalogues obtained from such galaxy samples are expected to have predominantly R-type underdense regions. Even though, these type of regions behaves on better agreement with linear theory, the brighter sample of galaxies is expected to trace the velocity field of high density structure, which has shown in this work have systematic departures from linearity at the inner regions. Therefore, it could be required a proper model of the velocity expansion profile of this systems when measurements are performed in redshift space. In the same direction, studies based on low redshift samples, as the main galaxy sample of the SDSS, can be benefited by an appropriate treatment of the velocity tracer population for both S- and R-type underdense regions.

ACKNOWLEDGMENTS

We thanks helpful comments and suggestions from the referee Paul Sutter, which have improved substantially the work presented. This work was partially supported by the Consejo Nacional de Investigaciones Científicas y Técnicas (CONICET), and the Secretaría de Ciencia y Tecnología (SeCyT), Universidad Nacional de Córdoba, Argentina. ANR acknowledges receipt of fellowships from CONICET. Plots are made using R software and post-processed with INKSCAPE.

REFERENCES

Aikio J., Mähönen P., 1998, ApJ, 497, 534
Aragón-Calvo M. A., Jones B. J. T., van de Weygaert R., van der Hulst J. M., 2007, A&A, 474, 315
Aragon-Calvo M. A., Szalay A. S., 2013, MNRAS, 428, 3409
Aragon-Calvo M. A., van de Weygaert R., Araya-Melo P. A., Platen E., Szalay A. S., 2010, MNRAS, 404, L89
Arbabi-Bidgoli S., Müller V., 2002, MNRAS, 332, 205
Babul A., Starkman G. D., 1992, ApJ, 401, 28
Barrow J. D., Bhavsar S. P., Sonoda D. H., 1985, MNRAS, 216, 17
Basilakos S., 2003, MNRAS, 344, 602
Benson A. J., Hoyle F., Torres F., Vogeley M. S., 2003, MNRAS, 340, 160
Bertschinger E., 1985, ApJS, 58, 1
Bertschinger E., 2001, ApJS, 137, 1
Bharadwaj S., Sahni V., Sathyaprakash B. S., Shandarin S. F., Yess C., 2000, ApJ, 528, 21
Biswas R., Alizadeh E., Wandelt B. D., 2010, Physical Review D, 82, 23002
Bond J. R., Kofman L., Pogosyan D., 1996, Nature, 380, 603
Bos E. G. P., van de Weygaert R., Dolag K., Pettorino V., 2012a, MNRAS, 426, 440
Bos E. G. P., van de Weygaert R., Ruwen J., Dolag K., Pettorino V., 2012b, arXiv:astro-ph/1211.3249
Brunino R., Trujillo I., Pearce F. R., Thomas P. A., 2007, MNRAS, 375, 184
Cai Y.-C., Li B., Cole S., Frenk C. S., Neyrinck M., 2014a, MNRAS, 439, 2978
Cai Y.-C., Neyrinck M. C., Szapudi I., Cole S., Frenk C. S., 2014b, ApJ, 786, 110
Cautun M., van de Weygaert R., Jones B. J. T., Frenk C. S., 2014, MNRAS, 441, 2923
Ceccarelli L., Padilla N., Lambas D. G., 2008, MNRAS, 390, L9
Ceccarelli L., Padilla N. D., Valotto C., Lambas D. G., 2006, MNRAS, 373, 1440
Ceccarelli L., Paz D., Lares M., Padilla N., Lambas D. G., 2013, MNRAS, 434, 1435
Clampitt J., Cai Y.-C., Li B., 2013, MNRAS, 431, 749
Colberg J. M., Krughoff K. S., Connolly A. J., 2005a, MNRAS, 359, 272
Colberg J. M. et al., 2008, MNRAS, 387, 933
Colberg J. M., Sheth R. K., Diaferio A., Gao L., Yoshida N., 2005b, MNRAS, 360, 216
Colless M. et al., 2001, MNRAS, 328, 10391063
Colless M. et al., 2003, arXiv:astro-ph/0306581
Costa-Duarte M. V., Sodré, Jr. L., Durret F., 2011, MNRAS, 411, 1716
Davis M., Efstathiou G., Frenk C. S., White S. D. M., 1985, ApJ, 292, 371
Doroshkevich A. G., 1970, Astrofizika, 6, 581
Dubinski J., da Costa L. N., Goldwirth D. S., Lecar M., Piran T., 1993, ApJ, 410, 458
Einasto M. et al., 2007, A&A, 476, 697
Eisenstein D. J. et al., 2011, AJ, 142, 72
El-Ad H., Piran T., 1997, ApJ, 491, 421
El-Ad H., Piran T., 2000, MNRAS, 313, 553
El-Ad H., Piran T., Dacosta L. N., 1997, MNRAS, 287, 790
Elyiv A., Marulli F., Pollina G., Baldi M., Branchini E., Cimatti A., Moscardini L., 2014, arXiv/astro-ph:1410.4559
Fillmore J. A., Goldreich P., 1984, ApJ, 281, 9
Forero-Romero J. E., Contreras S., Padilla N., 2014, MNRAS, 443, 1090
Foster C., Nelson L. A., 2009, ApJ, 699, 1252
Goldberg D. M., Jones T. D., Hoyle F., Rojas R. R., Vogeley M. S., Blanton M. R., 2005, ApJ, 621, 643
Górski K. M., Hivon E., Banday A. J., Wandelt B. D., Hansen F. K., Reinecke M., Bartelmann M., 2005, ApJ, 622, 759
Granett B. R., Neyrinck M. C., Szapudi I., 2008, ApJL, 683, L99
Hahn O., Porciani C., Carollo C. M., Dekel A., 2007, MNRAS, 375, 489
Hamaus N., Sutter P. M., Wandelt B. D., 2014a, Phys. Rev. L., 112, 251302
Hamaus N., Wandelt B. D., Sutter P. M., Lavaux G., Warren M. S., 2014b, Phys. Rev. L., 112, 041304
Hausman M. A., Olson D. W., Roth B. D., 1983, ApJ, 270, 351
Hernández-Monteagudo C., Smith R. E., 2013, MNRAS, 435, 1094
Hill G. J. et al., 2008, in Astronomical Society of the Pacific Conference Series, Vol. 399, Panoramic Views of Galaxy Formation and Evolution, Kodama T., Yamada T., Aoki K., eds., p. 115
Hoffman Y., Shaham J., 1982, ApJL, 262, L23
Hoyle F., Rojas R. R., Vogeley M. S., Brinkmann J., 2005, ApJ, 620, 618
Hoyle F., Vogeley M. S., 2002, ApJ, 566, 641
Hoyle F., Vogeley M. S., 2004, ApJ, 607, 751
Huchra J. et al., 2005, in ASP Conference Series, Vol. 329, Nearby Large-Scale Structures and the Zone of Avoidance, Fairall A. P., Woudt P. A., eds., p. 135
Huchra J. P., Geller M. J., 1982, ApJ, 257, 423
Icke V., 1984, MNRAS, 206, 1P
Ilić S., Langer M., Douspis M., 2013, A&A, 556, A51
Jarosik N. et al., 2011, ApJS, 192, 14
Kauffmann G., Fairall A. P., 1991, MNRAS, 248, 313
Kolokotronis V., Basilakos S., Plionis M., 2002, MNRAS, 331, 1020
Kruskal J. B., 1956, Proc. Amer. Math. Soc., 7, 48
Laigle C. et al., 2013, arXiv:astro-ph/1310.3801
Laureijs R. et al., 2011, arXiv:astro-ph/1110.3193
Lavaux G., Wandelt B. D., 2010, MNRAS, 403, 1392
Lavaux G., Wandelt B. D., 2012, ApJ, 754, 109
Libeskind N. I., Hoffman Y., Gottlöber S., 2014, MNRAS, 441, 1974
Luo S., Vishniac E., 1995, ApJS, 96, 429
Martel H., Wasserman I., 1990, ApJ, 348, 1
Mathis H., White S. D. M., 2002, MNRAS, 337, 1193
Melott A. L., Shandarin S. F., 1990, Nat., 346, 633
Micheletti D. et al., 2014, A&A, 570, A106
Müller V., Arbabi-Bidgoli S., Einasto J., Tucker D., 2000, MNRAS, 318, 280
Neyrinck M. C., 2008, MNRAS, 386, 2101

Padilla N. D., Ceccarelli L., Lambas D. G., 2005, MNRAS, 363, 977
Pápai P., Szapudi I., Granett B. R., 2011, ApJ, 732, 27
Park C., Choi Y.-Y., Kim J., Gott J. R., Kim S. S., Kim K.-S., 2012, ApJL, 759, L7
Patiri S. G., Betancort-Rijo J., Prada F., 2012, A&A, 541, L4
Patiri S. G., Betancort-Rijo J. E., Prada F., Klypin A., Gottlber S., 2006, MNRAS, 369, 335
Patiri S. G., Cuesta A. J., Prada F., Betancort-Rijo J., Klypin A., 2006, ApJL, 652, L75
Paz D., Lares M., Ceccarelli L., Padilla N., Lambas D. G., 2013, MNRAS, 436, 3480
Paz D. J., Lambas D. G., Padilla N., Merchán M., 2006, MNRAS, 366, 1503
Paz D. J., Sgró M. A., Merchán M., Padilla N., 2011, MNRAS, 414, 2029
Paz D. J., Stasyszyn F., Padilla N. D., 2008, MNRAS, 389, 1127
Peebles P. J. E., 1969, ApJ, 155, 393
Peebles P. J. E., 1976, ApJ, 205, 318
Peebles P. J. E., 2001, ApJ, 557, 495
Pellegrini P. S., da Costa L. N., de Carvalho R. R., 1989, ApJ, 339, 595
Pichon C., Bernardeau F., 1999, A&A, 343, 663
Platen E., van de Weygaert R., Jones B. J. T., 2007, MNRAS, 380, 551
Platen E., van de Weygaert R., Jones B. J. T., 2008, MNRAS, 387, 128
Plionis M., Basilakos S., 2002, MNRAS, 330, 399
Porciani C., Dekel A., Hoffman Y., 2002a, MNRAS, 332, 325
Porciani C., Dekel A., Hoffman Y., 2002b, MNRAS, 332, 339
Regos E., Geller M. J., 1991, ApJ, 377, 14
Rycroft C. H., 2009, Chaos, 19, 041111
Sahni V., Sathyaprakash B. S., Shandarin S. F., 1998, ApJL, 495, L5
Sathyaprakash B. S., Sahni V., Shandarin S., 1998, ApJ, 508, 551
Schneider M. D., Frenk C. S., Cole S., 2012, JCaP, 5, 30
Shandarin S., Feldman H. A., Heitmann K., Habib S., 2006, MNRAS, 367, 1629
Sheth J. V., Sahni V., Shandarin S. F., Sathyaprakash B. S., 2003, MNRAS, 343, 22
Sheth R. K., van de Weygaert R., 2004, MNRAS, 350, 517538
Slezak E., de Lapparent V., Bijaoui A., 1993, ApJ, 409, 517
Smargon A., Mandelbaum R., Bahcall N., Niederste-Ostholt M., 2012, MNRAS, 423, 856
Springel V., 2005, MNRAS, 364, 1105
Sutter P. M., Lavaux G., Wandelt B. D., Weinberg D. H., 2012, ApJ, 761, 187
Tavasoli S., Vasei K., Mohayaee R., 2013, A&A, 553, 15
Tegmark M. et al., 2004, ApJ, 606, 702
van Daalen M. P., Angulo R. E., White S. D. M., 2012, MNRAS, 424, 2954
van de Weygaert R., van Kampen E., 1993, MNRAS, 263, 481
Wang X., Szalay A., Aragón-Calvo M. A., Neyrinck M. C., Eyink G. L., 2014, ApJ, 793, 58
White S. D. M., 1984, ApJ, 286, 38
Zhang Y., Yang X., Wang H., Wang L., Mo H. J., van den Bosch F. C., 2013, ApJ, 779, 160